Decompression-induced condensation of carbon dioxide: Experiments, and prediction of the supercooling limit using classical nucleation theory

Morten Hammer[a,b,*], Alexandra Metallinou Log[a], Han Deng[a], Anders Austegard[a], Svend Tollak Munkejord[a]

[a] *SINTEF Energy Research, P.O. Box 4761 Torgarden, NO-7465 Trondheim, Norway*
[b] *Porelab, Department of Chemistry, Norwegian University of Science and Technology, NO-7491 Trondheim, Norway*

Abstract

This work investigates the nucleation of droplets from supercooled CO_2 and CO_2-rich gas during decompression, using classical nucleation theory (CNT). We model the supercooling limit employing highly accurate equations of state and compare the result with nucleation pressures determined from experimental data. The present analysis is relevant for the safety assessment of pipelines containing gaseous CO_2.

Three new full-bore decompression experiments with pure CO_2 were conducted, incorporating high-speed pressure sampling and multiple sensors to achieve precise characterization of the decompression wave speed as a function of pressure. Additionally, eight experiments with pure CO_2 and nine with CO_2-rich mixtures from the open literature were analysed.

The homogeneous equilibrium model (HEM) and delayed homogeneous equilibrium model (D-HEM) were used to calculate the decompression wave speed down to the choking condition. Across all experiments, predictions based on the saturation pressure (applied in the HEM) consistently overestimated the experimentally determined nucleation values. In contrast, those based on the supercooling limit (applied in D-HEM) showed a mean absolute percentage deviation of 3 %, with predictions randomly distributed around the experimental results.

Keywords: carbon dioxide, decompression, experiment, delayed condensation, classical nucleation theory, supercooling limit

1. Introduction

CO_2 capture and storage (CCS) has been identified as one of the key tools to mitigate climate change and reach the goals of the Paris agreement (Shukla *et al.*, 2022; IEA, 2022). As CO_2 capture and storage sites are typically not located in the same area, a CO_2 transport infrastructure will be needed. The CO_2 can be transported in several ways. However, for large CO_2 volumes there is a consensus that pipelines will be the most cost-effective (Smith *et al.*, 2021). Most CO_2 pipelines operating today transport the CO_2 in the dense phase, a single-phase state that, upon decompression, will approach the phase envelope from the liquid side. This is considered the most economical option (Roussanaly *et al.*, 2013).

For practical reasons, there is also interest in transportation of CO_2 in the gas phase. This may allow for the repurposing of old pipelines that cannot sustain the high pressures for dense phase transport. Carbon Limits and DNV (2021) found no showstoppers for the repurposing of existing offshore and onshore pipelines for gaseous CO_2 transport.

*Corresponding author.
Email address: morten.hammer@ntnu.no (Morten Hammer)

Another main case for pipe transport of CO_2 in the gas phase is for onshore pipes connecting emitters to ports, where the CO_2 can be sent to an offshore pipeline operating in the dense phase. Planned projects include the European Porthos project, where a 30 km long pipeline will be used for onshore transport of CO_2 through the Rotterdam area in the gaseous state at about 35 bar (Porthos, 2023). There are also several projects underway in China for the construction of CO_2 transmission pipelines (Bin *et al.*, 2024). Three of these are completed, all of which will transport the CO_2 in the gas phase.

For the safety assessment of pressurized pipelines, the decompression behaviour of the fluid inside the pipe must be known. This is relevant, e.g., for assessing the design limits with respect to the development of a running ductile fracture (RDF) in the pipe (Munkejord *et al.*, 2016). Several experimental and numerical studies have been conducted for the decompression of CO_2 and CO_2-rich mixtures in the dense phase. Examples include the studies conducted by Cosham *et al.* (2011, 2012, 2016); Drescher *et al.* (2014); Botros *et al.* (2016, 2017a,b,c); Michal *et al.* (2018); Munkejord *et al.* (2020, 2021); Log *et al.* (2024a). During the depressurization of CO_2 towards atmospheric pressure, phase change will occur. For decompression from the dense or liquid phase, the fluid will flash, creating bubbles. The pressure at which this phase change occurs is a key parameter in RDF assessment, and the current state of the art is to calculate the pressure assuming full thermodynamic equilibrium (Skarsvåg *et al.*, 2023; Michal *et al.*, 2020).

However, it has been well established in the literature for decompression from the dense phase that the phase change often occurs delayed, at a lower pressure than expected, see, e.g., Brown *et al.* (2013, 2014); Munkejord *et al.* (2020); Michal *et al.* (2020); Log *et al.* (2024a,b); Wilhelmsen and Aasen (2022). This is a non-equilibrium effect, and it is related to how the bubbles form. For decompression from the gas phase, the fluid will condense, forming droplets. There have been relatively few studies on CO_2 gas decompression (Cosham *et al.*, 2011; Mahgerefteh *et al.*, 2012; Cosham *et al.*, 2012). Nearly all of these studies have been conducted at the same initial pressure of 4 MPa. To the authors' knowledge, possible non-equilibrium effects for CO_2 gas decompression have not yet been studied or modelled. In order to gain insight on possible non-equilibrium effects, a more varied parameter space is needed. Therefore, three new pipe depressurization tests with different initial pressures have been conducted and are presented in this work. We further address the modelling of gas decompression with non-equilibrium condensation.

Phase transitions, such as condensation, cavitation, boiling and crystallization, often proceed through a process known as nucleation. However, in extreme cases where a gas is cooled far below its saturation temperature, phase transitions may proceed via spinodal decomposition, where density fluctuations grow spontaneously throughout the system. The rate-limiting step of nucleation involves the formation of a region of the new phase that reaches a critical size, enabling spontaneous growth of the new phase. This phenomenon forms the foundation of classical nucleation theory (CNT), a widely used framework for predicting the rates and properties of nucleating clusters (Debenedetti, 1997; Vehkamäki, 2006; Kashchiev, 2000). CNT can be used as a tool to predict phase change, by defining the large-scale phase change to occur at a critical nucleation rate of the new phase. For bubble formation, this is denoted the superheat limit. For condensation, we denote this the supercooling limit – the limit at which the gas cannot be cooled further before we observe the phase change.

While CNT provides a qualitative basis for understanding nucleation in pure fluids, it often falls short quantitatively, showing discrepancies as large as 7 orders of magnitude in predicted nucleation rates for a simple substance like argon (Wedekind *et al.*, 2007). Similarly, CNT predictions for multicomponent nucleation rates can be off by many orders of magnitude, and unphysical in the case of binary mixtures of water and strongly interacting molecules like alkanols. Aasen *et al.* (2020) showed that the erroneous negative number of particles in the critical embryo predicted by CNT in systems with strongly interacting molecules could be resolved by correcting for the curvature dependence in the surface tension. The curvature dependence of surface tension, including the Tolman length and the rigidity constants from the Helfrich expansion, is not readily available but can be estimated using classical density functional theory and density gradient theory (Aasen *et al.*, 2023). The limitations of the capillarity approximation have also been addressed through a generalization of the classical Gibbs

method, providing a more accurate description of the work of cluster formation down to the spinodal (Schmelzer *et al.*, 2000).

For a mixture of CO_2 and volatile impurities like hydrogen, nitrogen, oxygen, argon and methane, the binary interactions are weak, and CNT is expected to perform qualitatively well without curvature corrections, avoiding unphysical predictions like negative particle numbers in the critical embryo. The same applies to mixtures including the moderately polar sulfur dioxide molecule. At low degrees of supercooling, curvature corrections to the surface tension are expected to be small and can therefore be neglected. Although the CNT nucleation rates deviate by many orders of magnitude, the limits of superheat or supercooling are well predicted by CNT due to its exponential dependence on pressure, making it relatively insensitive to the critical nucleation rate (Debenedetti, 1997; Skarsvåg *et al.*, 2023).

Hammer *et al.* (2022) developed a delayed homogeneous equilibrium model, D-HEM, for decompressing flows. D-HEM is based on flow invariants and the CNT prediction of the limit of superheat in the case of bubble nucleation. Hammer *et al.* (2022) applied D-HEM to predict steady-state flow in nozzles and orifices for dense-phase CO_2. Later, the D-HEM formalism was extended to describe the decompression wave of CO_2-rich mixtures initially in the dense phase (Skarsvåg *et al.*, 2023). The D-HEM takes advantage of the fact that rapid decompression can be viewed as quasi steady from a process point of view. As a result, detailed spatial and temporal integration is not needed, and a full computational fluid dynamics (CFD) simulation is avoided. In the present work, the D-HEM is extended to pipe decompression of CO_2 and CO_2-rich gas mixtures by a droplet nucleation model based on CNT. However, instead of employing the CNT assumptions of ideal gas and incompressible liquid, we calculate the fluid properties using an equation of state.

The approach proposed in this work is general and can be applied to other systems with mixtures dominated by a single component, where droplets nucleate. By leveraging cross-disciplinary knowledge, we obtain valuable insights into the supercooling limit of CO_2 mixtures. Notably, our approach utilizes highly accurate equations of state to predict metastable fluid properties and introduces a model where the supercooling limit can be continuously plotted up to the critical point for fluid mixtures, offering a novel and comprehensive framework for studying nucleation phenomena.

One key impact we aim to achieve is to establish models incorporating supercooling limit predictions using CNT as a new standard for engineering and safety analysis in the assessment of ductile fracture propagation in pipelines. By advancing the understanding of nucleation phenomena and offering an accurate and simple framework for numerical predictions, we aim to contribute to more efficient pipeline design.

The remainder of the article is structured as follows. In Section 2, the experiments are briefly presented. In Section 3 the D-HEM for gas decompression is described. The results are presented in Section 4. Finally, concluding remarks are provided in Section 5.

2. Experiments

In this section, an overview of existing CO_2 gas decompression tests is provided. We then present the experimental facility, experimental procedure and initial conditions of the experiments conducted in the present work.

2.1. Previous experiments from literature

An overview of previous CO_2 gas decompression experiments available in the literature is shown in Table 1. Several tests have been conducted, both for pure CO_2 and CO_2-rich mixtures. The data with the highest resolution in terms of pressure sensor distribution and high frequency measurements are available from the tests of Munkejord *et al.* (2020) and Botros *et al.* (2017a). The remaining tests generally have fewer pressure sensors with lower frequency data recordings, and often only the depressurization wave speed is reported in the publications.

Table 1: Overview of full-bore decompression tests for pure CO_2 and CO_2-rich mixtures from an initial gaseous state or high-pressure gaseous-like state.

Reference	Name	Mixture composition (mol %)	P_0 (MPa)	T_0 (°C)
Munkejord *et al.* (2020) *	Test 3	100.0% CO_2	4.0	10.2
Cosham *et al.* (2011)	Test 02	100.0% CO_2	3.9	4.9
Cosham *et al.* (2011)†	Test 03	100.0% CO_2	3.9	5.1
Cosham *et al.* (2011)‡	Test 04	100.0% CO_2	3.9	20.2
Cosham *et al.* (2011) ‡	Test 13	100.0% CO_2	3.7	10.9
Cosham *et al.* (2011) ‡	Test 14	100.0% CO_2	3.7	10.9
Cosham *et al.* (2011)	Test 16	100.0% CO_2	3.9	5.0
Maxey (1983)**		100.0% CO_2	6.0	23.2
		CO_2 with impurities		
Cosham *et al.* (2011)	Test 05	97.0% CO_2, 3.0% H_2	3.9	5.1
Cosham *et al.* (2011)†	Test 06	96.0% CO_2, 4.0% N_2	3.8	5.3
Cosham *et al.* (2011)†	Test 07	99.1% CO_2, 0.9% SO_2	3.9	9.9
Cosham *et al.* (2011)	Test 08	95.7% CO_2, 3.3% H_2, 1.0% SO_2	3.9	10.0
Cosham *et al.* (2011)†	Test 09	94.8% CO_2, 4.2% N_2, 1.0% SO_2	3.9	10.0
Cosham *et al.* (2011)†	Test 10	88.9% CO_2, 7.9% N_2, 1.1% O_2, 1.1% CH_4, 1.0% SO_2	3.9	5.1
Cosham *et al.* (2011)	Test 11	89.4% CO_2, 3.2% H_2, 3.8% N_2, 1.3% O_2, 1.1% CH_4, 1.2% SO_2	3.7	16.3
Cosham *et al.* (2011)	Test 12	95.7% CO_2, 3.3% H_2, 1.0% SO_2	3.9	10.0
Botros *et al.* (2017a) *	Test #34	83.3% CO_2, 3.5% N_2, 5.8% O_2, 7.4 % Ar	13.4	59.1

* High resolution, high frequency pressure recordings.
** Initial density specified to 12.2 lb ft^{-3}.
† See also Mahgerefteh *et al.* (2012).
‡ See also Cosham *et al.* (2012).

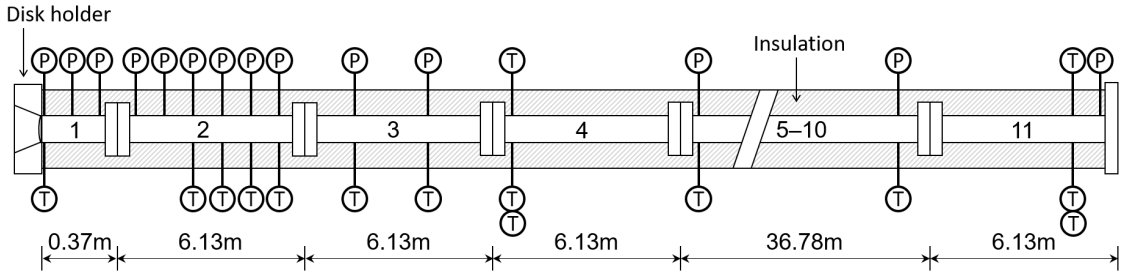

Figure 1: Test section (dimensions are not to scale; pipe no. 5–10 and corresponding sensors are omitted.)

2.2. The ECCSEL depressurization facility

The experiments of the present work were conducted at the ECCSEL depressurization facility. This facility has previously been employed by Munkejord *et al.* (2020, 2021); Log *et al.* (2024a,b). See Munkejord *et al.* (2020) for a more detailed description. A brief overview is provided here for completeness.

The ECCSEL depressurization facility (ECCSEL, 2023) has a test section consisting of a 61.67 m pipe made of stainless steel. The inner diameter of the pipe is 40.8 mm. A rupture disk with a disk holder is installed at the pipe outlet, and the pipe is densely instrumented with pressure and temperature sensors to capture the pressure transient once the rupture disk breaks. Figure 1 shows a schematic overview of the pipe.

In the present work, layered plastic rupture disks were applied to reach the intended initial pressure before disk rupture. During pressure build-up, the main focus was on following the desired isentropes to ensure that a sudden decompression would lead to phase change at different regions along the saturation curve.

Along the pipe, 16 fast-response pressure transducers of the type Kulite CTL-190(M) are flush-

Table 2: New full-bore decompression tests for pure CO_2.

Name	P_0 (MPa)	T_0 (°C)
Test 28	5.71	23.4
Test 30	6.39	36.4
Test 31	4.09	16.0

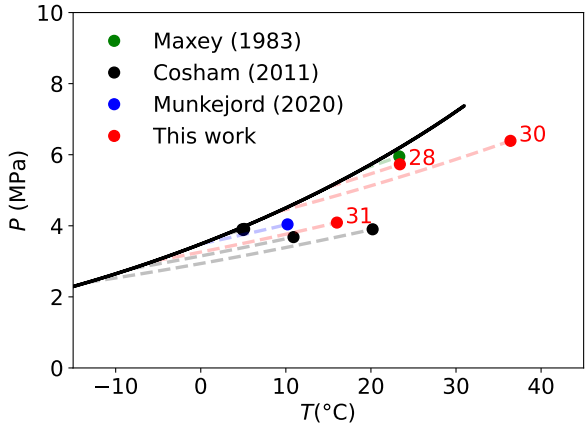

Figure 2: Pure CO_2 experiments. The dots represents the initial conditions of the experiments, and the dashed curves show the isentropic path down to the saturation curve. The test numbers are provided for the initial conditions of the present work.

mounted to the inner surface to capture the pressure transients during depressurization. The logging frequency of the data from the pressure transducers is 100 kHz, and for previous depressurization experiments the total measurement uncertainty has been estimated to be around 60 kPa. The high-frequency data are stored from 0.3 s before disk rupture for a 9 s period. The reported initial conditions of the experiments are calculated from the data between 1 ms and 0.5 ms before disk rupture.

2.3. New experiments conducted in this work

In the present work, three new CO_2 gas depressurization experiments were conducted. The initial conditions of the tests are summarized in Table 2. The conditions were chosen to complement the previous pure CO_2 gas decompression tests presented in Section 2.1, and to validate the nucleation predictions and the D-HEM for gas decompression tests by covering a range of relevant initial entropies. In particular, Test 28 and 30 cover initial entropies which have not been studied before, while Test 31 provides a reference for comparison with data from other sources. The initial temperature-pressure conditions of the new experiments are plotted alongside the initial conditions of previous pure CO_2 experiments in Figure 2. The figure also illustrates where the experiments intersect the saturation curve, assuming isentropic decompression.

2.4. Wave speed derived from the experimental data

The decompression wave speed is evaluated by considering the arrival time at the pressure sensors of given pressure levels from the depressurization wave, as described by Munkejord *et al.* (2020). The wave speed is found by linearly fitting the arrival times of the given pressure level at the pressure sensors as a function of their position. The pressure sensors should be located close together, to minimize the effect of friction, but enough sensors should be applied to obtain a good result despite varying sensor performance. In the present work, we chose to consider three sensors, at the positions

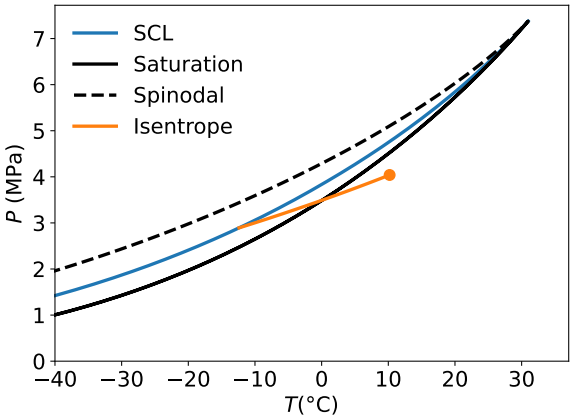

(a) Test 3 of Munkejord *et al.* (2020) with pure CO_2.

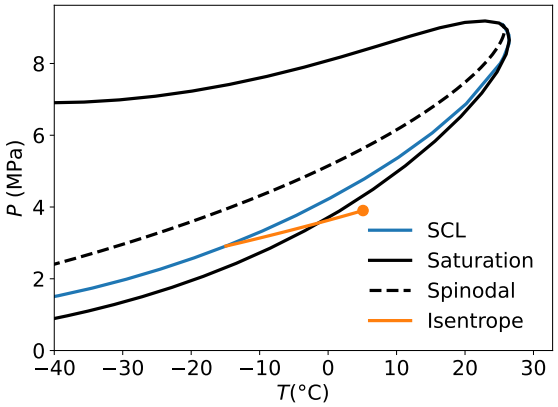

(b) Test 10 (88.9% CO_2, 7.9% N_2, 1.1% O_2, 1.1% CH_4, 1.0% SO_2) of Cosham *et al.* (2011).

Figure 3: Illustrations of the saturation curve together with the gas spinodal curve and the supercooling-limit (SCL) curve. The isentrope illustrates the isentropic decompression path down to the SCL curve. The initial condition of the decompression is shown as a dot.

8 cm, 28 cm and 80 cm from the open end of the pipe. These sensors provided consistent results for the experiments, while being close enough to avoid significant effects of friction.

3. The D-HEM for gas decompression

In order to utilize the D-HEM (Hammer *et al.*, 2022) to predict the decompression behaviour of pure CO_2 and CO_2-rich gas mixtures in a pipe, we develop a theory for the supercooling limit (SCL) based on classical nucleation theory (CNT). CNT is used to describe homogeneous droplet nucleation and is combined with the flow invariants of the Euler equations for 1D fluid flow to predict the depressurization behaviour.

Before delving into the model details, we provide an overview of the thermodynamic 'landscape', focusing on the temperature and pressure variations during the isentropic decompression. Figure 3a shows a pure CO_2 decompression case where fluid in an initially stable gaseous state at 4.0 MPa and 10.2 °C is isentropically cooled as the pressure drops in the pipeline. The isentrope illustrates the stable gas phase down to the saturation curve; beyond this point, it transitions into a metastable gaseous state until reaching the supercooling limit. The figure also includes the gas spinodal calculated from the equation of state (EOS), see Aursand *et al.* (2017) for details. Figure 3b shows the corresponding isentropic path for a CO_2-rich mixture initially at 3.9 MPa and 5.1 °C. This overview highlights the thermodynamic behaviour of CO_2 and CO_2-rich mixtures during decompression, illustrating the transitions from stable to metastable states along the isentropic path in temperature-pressure space. The figures also demonstrate the positioning of the supercooling limit and the gas spinodal relative to the saturation line.

3.1. Decompression wave speed

The decompression wave speed, $c - u$, is determined by the speed of sound of the rarefaction wave, c, relative to the flow velocity, u. This speed is found from the eigenvalues of the Euler equations, assuming one-dimensional flow. Under the isentropic conditions of the Euler equations, the result can be expressed as

$$c(P) - |u(P)| = c(P) - \int_P^{P_{\text{init}}} \frac{\mathrm{d}P'}{\rho(P')c(P')}, \tag{1}$$

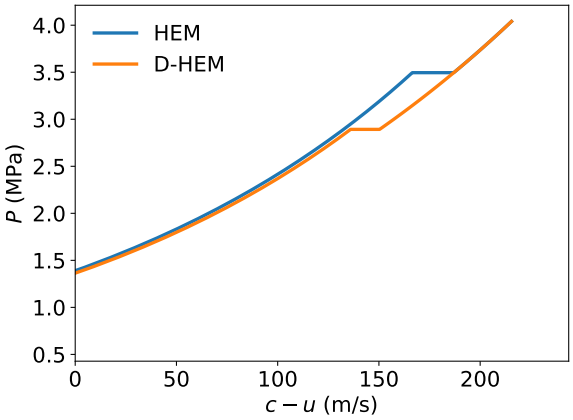

(a) Pure CO_2 gas experiment of Munkejord *et al.* (2020).

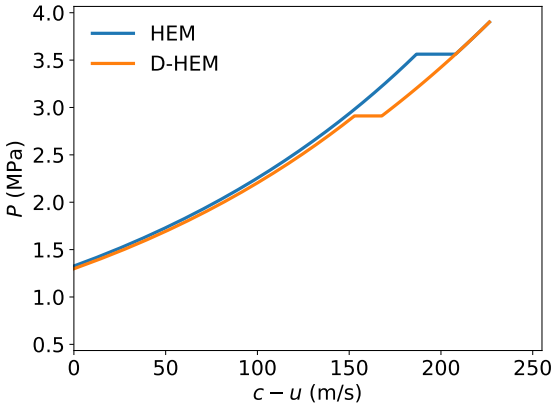

(b) Test 10 (88.9% CO_2, 7.9% N_2, 1.1% O_2, 1.1% CH_4, 1.0% SO_2) of Cosham *et al.* (2011).

Figure 4: Decompression wave speed curve calculated from Eq. (1).

where ρ is the mixed phase fluid density and P_{init} is the initial pressure. In the case of single-phase flow, the properties in Eq. (1) are straightforward to calculate from an EOS. However, for two-phase flow, the situation becomes more complicated. In this case, the speed of sound calculated for the two-phase mixture depends on the assumptions made in the flow model. The decompression wave speed from the initial state in a pipe to the choking flow condition is applied in engineering methods to assess design criteria to avoid running ductile fracture in pipes (Skarsvåg *et al.*, 2023; Michal *et al.*, 2020). The current state of the art in these models is to apply the homogeneous equilibrium model in calculating the decompression speed in a two-phase state.

In the derivation of the above expression for the homogeneous equilibrium flow model (HEM), full mechanical and thermodynamic equilibrium is assumed, i.e., for a two-phase state, the phases have the same velocity, pressure, temperature and chemical potential. These assumptions lead to a discontinuous speed of sound at the phase boundary, see Hammer *et al.* (2022), and further, to a jump in the decompression-wave speed as a function of pressure. Hammer *et al.* (2022) introduced the delayed homogeneous equilibrium model, D-HEM, which accounts for a possible delay in the phase change. In the case of the D-HEM for gas decompression, the jump in decompression-wave speed is shifted from the saturation state to the supercooling limit. As an example, Figure 4 shows calculated decompression wave speeds, employing both HEM and D-HEM, for the experiments of Figure 3. The discontinuity in the speed of sound when droplets form appears as an isobaric plateau in the figure. The experiments are not expected to display true discontinuities, but nevertheless to show clear change in the decompression wave speed allowing for the identification of droplet nucleation. In the figure, the decompression curve is plotted down to $c - u = 0$, known as the choking condition.

3.2. Droplet nucleation model

In order to estimate the liquid supercooling limit, we seek to establish a droplet nucleation model. Condensation is an activated process occurring via the formation of a droplet that reaches a critical size within a supercooled gas. In the framework of CNT, the nucleation rate is expressed as an Arrhenius equation (Vehkamäki, 2006; Aasen *et al.*, 2023),

$$J = J_0 \exp\left(\frac{-W_*}{k_B T}\right) \tag{2}$$

where W_* is the work associated with the formation of critically sized droplet, k_B is the Boltzmann constant and T is the temperature. The prefactor is given by

$$J_0 = \beta_* C Z, \tag{3}$$

where β_* is the condensation coefficient, C is the normalization factor of the cluster size distribution and, Z, is the Zeldovich factor. The equations defining β_*, C, and Z will be provided later in this section.

In CNT, simplifying assumptions of ideal gas and incompressible liquid are typically applied, but the fluid phases can easily be described using an EOS. With a suitable Helmholtz-free-energy-based EOS, the chemical potentials of the phases ($\boldsymbol{\mu}$) and the pressure (P) will be consistently described from thermodynamic differentials given the temperature and molecular densities ($\boldsymbol{\rho}$). In the following, the gas and liquid phase are denoted using the subscripts g and ℓ, respectively. In addition, bold symbols are used to represent vector quantities.

The nucleation rate is calculated for states where the bulk gas and the droplet are in chemical equilibrium. This equilibrium criterion is defined by the following equation,

$$\boldsymbol{\mu}(T, \boldsymbol{\rho}_g) = \boldsymbol{\mu}(T, \boldsymbol{\rho}_\ell). \tag{4}$$

Given the molecular density of the gas, $\boldsymbol{\rho}_g$, the droplet molecular density, $\boldsymbol{\rho}_\ell$, can be calculated. The pressure of the phases are calculated from the EOS by

$$P_k = P(T, \boldsymbol{\rho}_k), \ k \in g, \ell. \tag{5}$$

For a perfectly spherical droplet, the work of formation for the critical droplet is (Vehkamäki, 2006; Kashchiev, 2000),

$$W_* = \frac{4\pi}{3}\sigma r_*^2, \tag{6}$$

where σ denotes the surface tension of the droplet. The droplet radius is under the capillary approximation calculated from the Laplace equation as (Aasen *et al.*, 2020; Kashchiev, 2000)

$$r_* = \frac{2\sigma}{P_\ell - P_g}. \tag{7}$$

The condensation coefficient (β_*) represents the likelihood that a cluster will grow upon collision with a monomer (gas molecule). In typical gases, monomers are far more numerous than clusters, making monomer-cluster collisions much more frequent than cluster-cluster collisions, which can thus be neglected. It is also assumed that clusters lose mass only through the detachment of single monomers. Note that we are here considering a multicomponent mixture. The probability of successful adhesion to a cluster depends on both the concentration of monomers of component i, and the monomer-cluster collision frequency ($\bar{\beta}_{*,i}$) (Vehkamäki, 2006),

$$\beta_{*,i} = \frac{1}{v_{g,i}}\bar{\beta}_{*,i}, \tag{8}$$

where we follow the common practice of using the ideal gas assumption, $v_{g,i}^{-1} = y_i P_g / k_B T$, when calculating the concentration of monomers of component i. Here, y_i is the mole fraction of component i in the gas phase.

According to kinetic gas theory, the collision frequency of type i monomers with clusters ($*$) is given by Friedlander (2000) as

$$\bar{\beta}_{*,i} = \left(\frac{3}{4\pi}\right)^{1/6} \sqrt{\frac{6k_B T}{m_*} + \frac{6k_B T}{m_i}} \left(V_*^{1/3} + v_{\ell,i}^{1/3}\right)^2, \tag{9}$$

where m is the weight. The partial molar (molecular) volume of the liquid phase is calculated from the EOS using

$$v_{\ell,i} \equiv \left.\frac{\partial V_\ell}{\partial N_i}\right|_{N_j,T,P}, \tag{10}$$

where V is volume and N is the number of molecules.

As an approximation to the condensation coefficient of the mixture, we simply average the values from Eq. (8) to obtain an overall condensation coefficient of the droplet,

$$\beta^* = \frac{1}{\mathcal{N}} \sum_{i=1}^{\mathcal{N}} \beta_{*,i}. \tag{11}$$

For the pure fluid case, the above expression reduces to the theoretically correct value. For the cases considered in this work, the CO_2 concentration is larger than or equal to 88.9 %. We therefore expect the above simplification to be reasonable. Generally, the average growth rate of a multicomponent mixture droplet is dependent on the direction of droplet growth in the size-composition plane (Stauffer, 1976; Ohta, 1982; Trinkaus, 1983; Vehkamäki and Ford, 2000), but this will not be pursued in this work.

In their work on binary nucleation, Wilemski and Wyslouzil (1995) proposed a normalization factor of the cluster size distribution, C, depending on the bulk phase molecular densities. For a pure fluid, the term reduces to the molecular density. In this work we approximate the normalization factor using the ideal-gas molecular density, motivated by the single-component expression used by Vehkamäki (2006),

$$C = \frac{P_\mathrm{g}}{k_\mathrm{B} T}. \tag{12}$$

The Zeldovich factor, Z, using the concept of virtual monomer volume becomes (Kulmala and Viisanen, 1991),

$$Z = \sqrt{\frac{\sigma}{k_\mathrm{B} T}} \frac{v_\ell}{2\pi r_*^2}. \tag{13}$$

For a given temperature, one must decide on a critical nucleation rate that represents the observed sudden phase change. The exact value of the critical nucleation rate (J_crit) has little influence on the predicted limit of superheat for bubble nucleation (Debenedetti, 1997). The same applies to the SCL for CO_2 droplets, as can be seen in the results section.

Given temperature, gas composition, $\boldsymbol{y}$ and critical nucleation rate, Eq. (2) can be solved for the gas mixture density, ρ_g,

$$J(T, \boldsymbol{y}\rho_\mathrm{g}) = J_\mathrm{crit} \tag{14}$$

to determine the SCL. Figure 5 shows the SCL for pure CO_2 together with the saturation curve and the gas spinodal calculated from the EOS. Here, Figure 5a provides a pressure-temperature plot including the predicted droplet pressure, while Figure 5b gives a temperature-density plot including the predicted density of the critically-sized droplets.

3.3. Thermophysical models

The most accurate equations of state that can be applied for the modelling of CO_2 and CO_2-rich mixtures today are the EOS-CG (Gernert and Span, 2016; Neumann *et al.*, 2023) and the GERG-2008 EOS (Kunz and Wagner, 2012). EOS-CG has been tuned specifically for mixtures of CO_2 with relevant gases produced during combustion. The GERG-2008 EOS is made for natural gas mixtures, but is also accurate for CO_2 mixtures. These multiparameter EOSs have unparalleled accuracy in the stable regions of the phase diagram. However, the presence of a second Maxwell loop renders their predictions unreliable in the metastable and unstable region (Hammer *et al.*, 2024). The second Maxwell loop seems to be an artefact of the functional form and parameterization (Wilhelmsen *et al.*, 2017).

Despite these deficiencies, we have chosen to use the GERG-2008 EOS in this work due to its accurate density predictions. Since the GERG-2008 EOS behaves slightly better than EOS-CG in the metastable

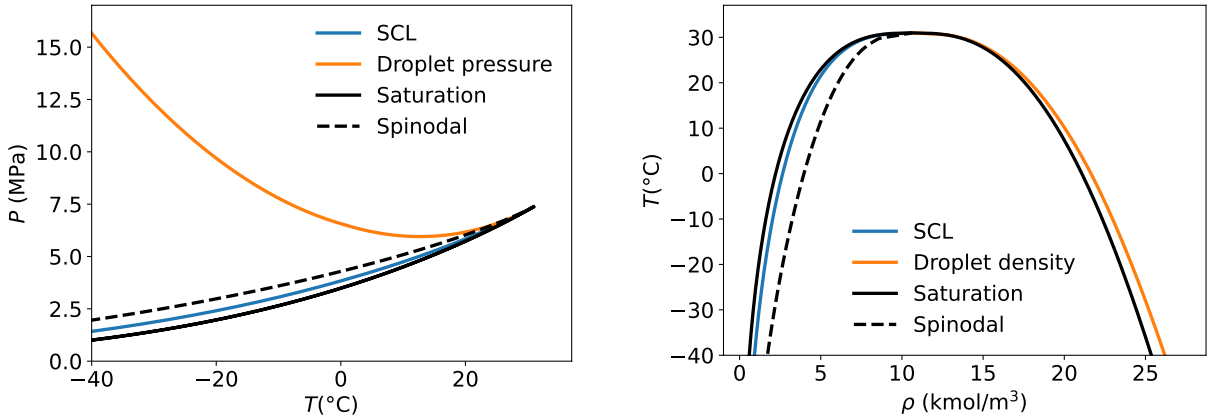

(a) Pressure-temperature space.

(b) Temperature-density space.

Figure 5: Pure CO_2 saturation curve (black), the supercooling-limit curve (SCL) for the droplet nucleation (blue), the gas spinodal (dashed black) and the equilibrium properties of the critically sized droplet (orange, see Equation (4) and (5)) are shown. The SCL is shown for a nucleation rate of $J_{\text{crit}} = 10^{14} \text{m}^{-3}\,\text{s}^{-1}$.

region, it is easier to work with numerically. As the droplet nucleation state at the supercooling limit is fairly close to the saturation state, as illustrated in Figure 5b, reasonable accuracy can be expected with the EOS. To include SO_2 with GERG-2008, we extend the model using the multiparameter model of Gao *et al.* (2016), and the binary interactions models of EOS-CG (Herrig, 2018; Neumann *et al.*, 2023). The accuracy of property predictions in the metastable region of the EOS is difficult to quantify. However, given that these models are accurate to experimental precision in the stable region, they are expected to extrapolate with good accuracy into the metastable region near the saturation curve.

To estimate the surface tension of CO_2 mixtures, we employ the parachor method (Sugden, 1924; Weinaug and Katz, 1943; Hugill and Van Welsenes, 1986). The surface tension is then estimated as

$$\sigma_{\text{mix}} = \left(\mathcal{P}_\ell \rho_\ell - \mathcal{P}_g \rho_g\right)^m, \tag{15}$$

where $\mathcal{P}_k$ denotes the parachor of phase k,

$$\mathcal{P}_\ell = \sum_{i=1}^{n}\sum_{j=1}^{n} x_i x_j \mathcal{P}_{ij}, \text{ and } \mathcal{P}_g = \sum_{i=1}^{n}\sum_{j=1}^{n} y_i y_j \mathcal{P}_{ij} \tag{16}$$

and

$$\mathcal{P}_{ij} = (1 - \delta_{ij})\frac{\mathcal{P}_i + \mathcal{P}_j}{2}, \tag{17}$$

where δ_{ij} is a binary interaction parameter, x_i and y_i are the molar compositions of the liquid and gas phases, respectively. m is set to 3.87, as applied in REFPROP v10 (Log *et al.*, 2023). We use the pure fluid correlations of Mulero *et al.* (2012) to estimate the pure fluid parachors as a function of temperature:

$$\mathcal{P}_i = \frac{\sigma_i(T)^{1/m}}{\rho_\ell - \rho_g}. \tag{18}$$

For this work, we assume ideal mixing, i.e., the binary interaction parameter is set to zero ($\delta_{ij} = 0$). To the best of the authors' knowledge, no relevant binary experimental data are available for carbon dioxide and the other species, making us unable to correlate the most important interaction parameters.

4. Results and discussion

In this section, we present the results of our investigation into the modelling of the supercooling limit, comparing with data from decompression experiments. The first subsection examines the sensitivity of the supercooling limit to the critical nucleation rate, exploring how variations in this rate affect the overall behaviour of the system. In the second subsection, we focus on the prediction of the supercooling limit, comparing the outcomes from the CNT-based model, evaluating its accuracy in capturing experimental observations. Together, these analyses provide a deeper understanding of the role of nucleation rates and modelling approaches in determining the supercooling limit during decompression processes.

4.1. Sensitivity to the supercooling limit determined by the critical nucleation rate.

Figure 6 shows the supercooling limit for pure CO_2 together with the saturation curve calculated from the EOS. Figure 6a shows a pressure-temperature plot, while Figure 6b shows a temperature-density plot. In both plots the sensitivity to the value of the critical nucleation rate is illustrated by plotting the supercooling limit for three different rates, $J_{\text{crit}} = 10^6/\text{m}^3\text{s}$, $J_{\text{crit}} = 10^{12}/\text{m}^3\text{s}$ and $J_{\text{crit}} = 10^{18}/\text{m}^3\text{s}$. As can be seen, the SCL is nearly insensitive to the choice of critical nucleation rate. The insensitivity is due to the exponential behaviour of the nucleation rate. This is similar to what is observed for the critical nucleation rate when predicting the limit of superheat for bubble nucleation (Debenedetti, 1997).

4.2. Prediction of the supercooling limit

Figure 7 illustrates the decompression speed for the experiments conducted in this campaign. The experimental decompression speeds are compared with the calculated results from the HEM and D-HEM. In the D-HEM, the pressure plateau lies below that of the HEM due to delayed droplet nucleation and the metastable path down to the supercooling limit. The experimentally derived nucleation pressure is indicated by a red star; however, it is associated with some uncertainty as the experimental data do not exhibit a distinct plateau, but rather a change in gradient. Quantifying the uncertainty in the experimental decompression curve is challenging, as it depends on averaging data from three sensors to determine the speed of the rarefaction wave travelling in the pipe. Deriving the nucleation pressure from the decompression curve involves detecting when the gradient of pressure

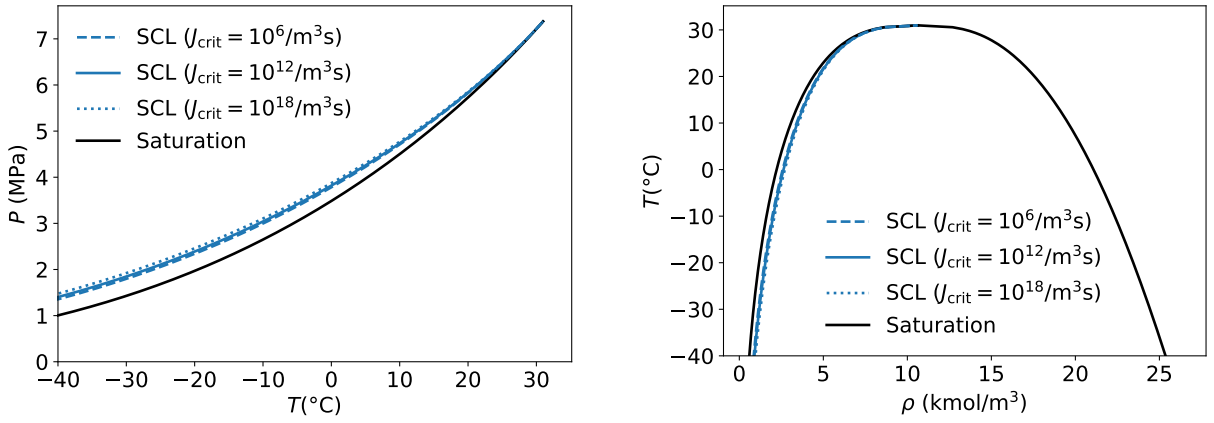

(a) Pressure-temperature space.

(b) Temperature-density space.

Figure 6: Pure CO_2 saturation curve (black), the supercooling-limit curve (SCL) for the droplet nucleation (blue) plotted for three choices of critical nucleation rates, $J_{\text{crit}} = 10^6/\text{m}^3\text{s}$ (dashed), $J_{\text{crit}} = 10^{12}/\text{m}^3\text{s}$ (solid) and $J_{\text{crit}} = 10^{18}/\text{m}^3\text{s}$ (dotted).

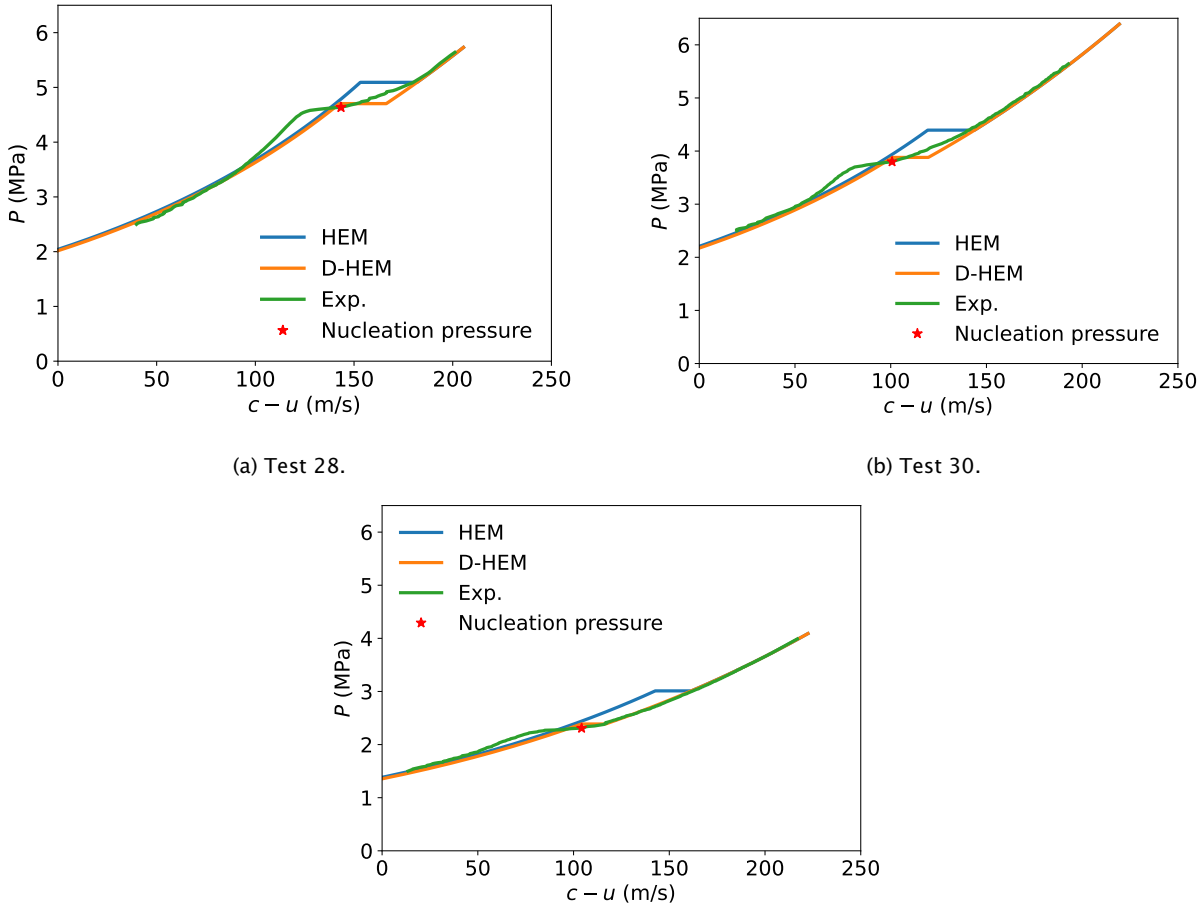

(a) Test 28.

(b) Test 30.

(c) Test 31.

Figure 7: Decompression speeds of new experiments (green), compared to HEM (blue) and D-HEM (orange) calculations. The experimentally derived nucleation pressure is indicated as a red star.

with respect to decompression velocity undergoes a substantial change. The nucleation pressure is then determined by the intersection of the linear curve fits for the points directly above and below the detected discontinuity in the gradient.

All experiments show an initial undershoot of the two-phase equilibrium decompression speed below the supercooling limit, before relaxing towards the modelled decompression speed at lower pressures. Whether this behaviour results from a physical process or is an artefact of the averaging procedure in our calculation of the wave speed remains unclear. Notably, in the case of Test 31 the experimental decompression curve follows the metastable path (D-HEM) perfectly before two-phase flow is observed. For both Test 28 and Test 30, there is a more gradual transition toward the two-phase branch. In all cases, the CO_2 gas decompression experiments show clear non-equilibrium in the transition from single to two-phase flow.

Table 3 summarizes all the available decompression experiments of CO_2-rich mixtures, presenting the nucleation pressure derived from experimental data, the saturation pressure (HEM) and the supercooling limit for isentropic decompression (D-HEM). Both models are compared to the experimental nucleation pressure, with deviations reported as percentages (%). The results show that the saturation pressure consistently overpredicts the nucleation pressure, whereas the supercooling limit aligns

Table 3: Summary of decompression experiments for CO_2-rich mixtures, showing nucleation pressure, saturation pressure (sat), and the supercooling limit (SCL), with deviations from experimental values reported as percentages (%). The pure CO_2 experiments are show at the top of the table while the CO_2-rich mixtures are show at the bottom of the table.

Ref	Name	P_N (MPa)	P_{sat} (MPa)	ε_{sat} (%)	P_{SCL} (MPa)	ε_{SCL} (%)
This work	Test 28	4.64	5.09	9.84	4.70	1.46
This work	Test 30	3.80	4.39	15.6	3.88	2.12
This work	Test 31	2.31	3.01	30.3	2.39	3.36
Munkejord *et al.* (2020)	Test 3	2.87	3.50	21.9	2.89	0.89
Cosham *et al.* (2011)	Test 02	3.35	3.83	14.3	3.25	-2.91
Cosham *et al.* (2011)	Test 03	3.23	3.83	18.4	3.25	0.57
Cosham *et al.* (2011)	Test 04	1.89	2.41	27.6	1.79	-4.90
Cosham *et al.* (2011)	Test 13	1.99	2.79	40.2	2.17	8.90
Cosham *et al.* (2011)*	Test 14	2.19	2.79	27.7	2.17	-0.81
Cosham *et al.* (2011)	Test 16	3.20	3.77	17.7	3.19	-0.42
Maxey (1983)		5.26	5.59	6.15	5.29	0.59
		CO_2 with impurities				
Cosham *et al.* (2011)	Test 05	2.83	3.60	27.2	3.00	6.10
Cosham *et al.* (2011)	Test 06	2.83	3.50	23.5	2.88	1.93
Cosham *et al.* (2011)	Test 07	2.81	3.53	25.9	2.93	4.30
Cosham *et al.* (2011)	Test 08	2.84	3.40	19.6	2.78	-2.08
Cosham *et al.* (2011)	Test 09	2.57	3.37	28.0	2.74	4.02
Cosham *et al.* (2011)	Test 10	2.72	3.56	30.8	2.91	6.86
Cosham *et al.* (2011)	Test 11	2.71	3.66	35.0	3.01	11.0
Cosham *et al.* (2011)	Test 12	1.77	2.38	34.9	1.77	0.28
Botros *et al.* (2017a)	Test #34	7.02	7.45	6.14	7.26	3.45

* Two plateaus are observed; the lowest plateau is reported. Errors with the highest plateau value for the saturation and the supercooling limit are 7.0 % and −16.9 %, respectively.

closely with the experimental data. The deviations between the experimentally derived nucleation pressure and model predictions are illustrated in Figure 8.

Plots of decompression speed for the previous experiments found in the literature are provided in Appendix A. Based on all experimentally derived nucleation pressures, the magnitude of the critical nucleation rate was adjusted to $J_{crit} = 10^{14} \mathrm{m}^{-3}\,\mathrm{s}^{-1}$, a relatively high value. This choice yielded slightly better results compared to using smaller values. With this choice of critical nucleation rate, the mean absolute percentage deviation (MAPD) of the calculated supercooling limit compared to the experimentally derived nucleation pressure across all experiments is 3 %. In comparison, the MAPD of the calculated saturation pressure compared to the experimentally derived nucleation pressure across all experiments is 23 %.

The reduced agreement between the model and the CO_2-mixture experimental results raises questions about the applicability of the simple approximation for the condensation coefficient. However, multiple sources of uncertainty make it challenging to attribute the offset solely to this assumption without more detailed experiments. For mixtures, additional uncertainty arises from the predicted mixture surface tension, compounded by uncertainties in the calculation of the decompression curve, as observed for pure CO_2 as well. These uncertainties include the averaging of noise in pressure measurements and variability in initial conditions.

In Tests 04 and 14 of Cosham *et al.* (2011), some wobbling is observed in the experimental pressure versus decompression-speed curves, see Figure A.2. This behaviour may result from noise in the pressure measurements, uncertainties in the calculation of decompression speed, or inhomogeneities in the pipe fluid. For Test 04, temperature inhomogeneity could be a contributing factor, while for Test 14, both temperature and compositional inhomogeneity are potential causes.

Figure 8 illustrates the deviations between the experimentally derived nucleation pressure, the predicted saturation pressure and the supercooling-limit pressure. The saturation pressure consistently overpredicts the nucleation pressure across all cases, with the relative deviation increasing as the

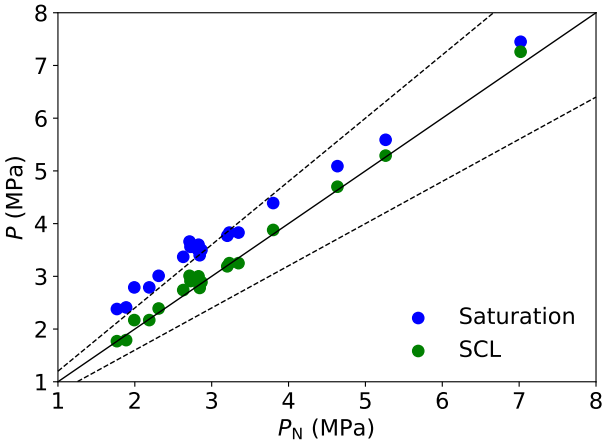

Figure 8: Saturation pressure (blue) and the supercooling-limit pressure (green) are plotted against the experimentally derived nucleation pressure for all experiments listed in Table 3. Dashed black lines indicate deviations of ±20 %, while the solid black line represent 0 % deviation.

nucleation pressure decreases. In contrast, the deviations in the supercooling-limit pressure predictions appear to be randomly distributed.

5. Conclusion

This study employs classical nucleation theory (CNT) to describe the nucleation of droplets from supercooled CO_2 and CO_2-rich gases during decompression. Employing highly accurate equations of state and parachor-based surface tension predictions, we have determined the supercooling limit and compared it with experimentally observed nucleation pressures from CO_2 pipe decompression tests. Consistent with findings for the limit of superheat in bubble nucleation, the predicted supercooling limit was found to be relatively insensitive to variations in the critical nucleation rate.

During the decompression of a pipe, a rarefaction wave propagates inward from the open end, with each pressure level having its own pressure-propagation wave speed. This characteristic behaviour can be visualized as a decompression curve. When droplet nucleation begins, a plateau or a change in gradient is typically observed in the curve, marking the point where nucleation becomes predominant. Assuming isentropic flow in the pipe, we have calculated the decompression speed using invariants of the Euler equations. Along the isentrope, we have identified both the saturation pressure and the supercooling-limit pressure.

This work presents three new experiments involving full-bore depressurizations of a pipe initially filled with pure CO_2. The initial conditions were chosen to complement eight experiments already reported in the literature. The experiments were conducted with high-speed pressure sampling and multiple pressure sensors near the pipe's open end, enabling precise characterization of the decompression curve. In addition to the pure CO_2 experiments, experiments with nine CO_2-rich mixtures, containing at least 88.9 % CO_2, are analysed and compared with model predictions. These mixtures include a range of impurities such as volatile gases (hydrogen, nitrogen, oxygen, argon and methane) and sulfur dioxide.

The full decompression curves, extending to the choking condition (zero velocity), were plotted for all available experiments using the homogeneous equilibrium model (HEM) and the delayed homogeneous equilibrium model (D-HEM). The mean absolute percentage deviation (MAPD) of the supercooling limit applied in the D-HEM was 3 % across all experiments. The saturation pressure applied in the HEM systematically overpredicted the nucleation pressure with an MAPD of 23 %, whereas

the supercooling-limit predictions appear randomly distributed around the nucleation pressure found in the experiments.

The high accuracy of CNT in predicting nucleation pressure makes D-HEM a valuable tool for evaluating design limits related to the onset of running ductile fractures in pipelines transporting CO_2 in a gas-like state.

Acknowledgments

This work was part of the NCCS Centre, funded by the Centres for Environment-friendly Energy Research (FME) programme of the Research Council of Norway (257579) and supported by Aker BP, SLB Capturi, Allton, Ansaldo Energia, Baker Hughes, CoorsTek Membrane Sciences, Elkem, Eramet, Equinor, Gassco, Hafslund Oslo Celsio, Krohne, Larvik Shipping, Norcem Heidelberg Cement, Offshore Norge, Quad Geometrics, Stratum Reservoir, TotalEnergies, Vår Energi and Harbour Energy.

Part of the work was performed in the COREu project, having received funding from the European Union's HE research and innovation programme under grant agreement id. 101136217.

The construction of the ECCSEL Depressurization Facility was supported by the INFRASTRUKTUR programme of the Research Council of Norway (225868).

The work was also partly supported by the Research Council of Norway through its Centres of Excellence funding scheme, Porelab, project number 262644 and the European Research Council project, InterLab, under grant agreement id. 101115669.

Data availability

The experimental data acquired in this study are available at Zenodo (Hammer *et al.*, 2025).

References

Aasen, A., Reguera, D., Wilhelmsen, Ø., Jan. 2020. Curvature corrections remove the inconsistencies of binary classical nucleation theory. *Phys. Rev. Lett.* 124 (4), 045701. doi:10.1103/physrevlett.124.045701.

Aasen, A., Wilhelmsen, Ø., Hammer, M., Reguera, D., Mar. 2023. Free energy of critical droplets – from the binodal to the spinodal. *J. Chem. Phys.* 158 (11). doi:10.1063/5.0142533.

Aursand, P., Gjennestad, M. A., Aursand, E., Hammer, M., Wilhelmsen, Ø., 2017. The spinodal of single- and multi-component fluids and its role in the development of modern equations of state. *Fluid Phase Equilib.* 436, 98–112. doi:10.1016/j.fluid.2016.12.018.

Bin, L., Kaixuan, L., Zhipeng, Y., Zaizhou, W., Wenjun, C., 2024. A study on decompression wave propagation characteristics during CO_2 pipeline leakage with consideration of gas-liquid transition. *Greenhouse Gases: Science and Technology* 14 (4), 575–586. doi:https://doi.org/10.1002/ghg.2283.

Botros, K. K., Geerligs, J., Rothwell, B., Robinson, T., Jun. 2016. Measurements of decompression wave speed in pure carbon dioxide and comparison with predictions by equation of state. *J. Press. Vess. – T. ASME* 138 (3). doi:10.1115/1.4031941.

Botros, K. K., Geerligs, J., Rothwell, B., Robinson, T., Mar. 2017a. Effect of argon as the primary impurity in anthropogenic carbon dioxide mixtures on the decompression wave speed. *Can. J. Chem. Eng.* 95 (3), 440–448. doi:10.1002/cjce.22689.

Botros, K. K., Geerligs, J., Rothwell, B., Robinson, T., Apr. 2017b. Measurements of decompression wave speed in binary mixtures of carbon dioxide mixtures and impurities. *J. Press. Vess. – T. ASME* 139 (2). doi:10.1115/1.4034016.

Botros, K. K., Geerligs, J., Rothwell, B., Robinson, T., Apr. 2017c. Measurements of decompression wave speed in simulated anthropogenic carbon dioxide mixtures containing hydrogen. *J. Press. Vess. – T. ASME* 139 (2). doi:10.1115/1.4034466.

Brown, S., Martynov, S., Mahgerefteh, H., Chen, S., Zhang, Y., 2014. Modelling the non-equilibrium two-phase flow during depressurisation of CO_2 pipelines. *Int. J. Greenh. Gas Con.* 30, 9–18. doi:10.1016/j.ijggc.2014.08.013.

Brown, S., Martynov, S., Mahgerefteh, H., Proust, C., 2013. A homogeneous relaxation flow model for the full bore rupture of dense phase CO_2 pipelines. *Int. J. Greenh. Gas Con.* 17, 349–356. doi:10.1016/j.ijggc.2013.05.020.

Carbon Limits and DNV, Oct. 2021. Re-stream – study on the reuse of oil and gas infrastructure for hydrogen and CCS in Europe. DNV-RP-F104. URL `https://www.concawe.eu/wp-content/uploads/Re-stream-final-report_Oct2021.pdf`.

Cosham, A., Jones, D., Barnett, J., Jun. 2011. The decompression behaviour of CO_2 in the gas phase. In: *International Forum on the Transportation of CO_2 by Pipeline*. Clarion Technical Conferences, Gateshead, UK.

Cosham, A., Jones, D. G., Armstrong, K., Allason, D., Barnett, J., 24–28 Sep 2012. Ruptures in gas pipelines, liquid pipelines and dense phase carbon dioxide pipelines. In: *9th International Pipeline Conference, IPC2012*. ASME, IPTI, Calgary, Canada, vol. 3, pp. 465–482. doi:10.1115/IPC2012-90463.

Cosham, A., Jones, D. G., Armstrong, K., Allason, D., Barnett, J., 26–30 Sep 2016. Analysis of a dense phase carbon dioxide full-scale fracture propagation test. In: *11th International Pipeline Conference, IPC2016*. Calgary, Canada, vol. 3. doi:10.1115/IPC2016-64456.

Debenedetti, P. G., 1997. *Metastable Liquids: Concepts and Principles*. Princeton University Press. ISBN 9780691213941. doi:10.1515/9780691213941.

Drescher, M., Varholm, K., Munkejord, S. T., Hammer, M., Held, R., de Koeijer, G., Oct. 2014. Experiments and modelling of two-phase transient flow during pipeline depressurization of CO_2 with various N_2 compositions. In: Dixon, T., Herzog, H., Twinning, S. (Eds.), *GHGT-12 – 12th International Conference on Greenhouse Gas Control Technologies*. University of Texas at Austin / IEAGHGT, Energy Procedia, vol. 63, Austin, Texas, USA, pp. 2448–2457. doi:10.1016/j.egypro.2014.11.267.

ECCSEL, 2023. Depressurization facility. `https://eccsel.eu/catalogue/facility/?id=113`. Accessed 2023-05-23.

Friedlander, S. K., 2000. *Smoke, Dust and Haze: Fundamentals of Aerosol Behavior*. Topics in Chemical Engineering. Oxford University Press, New York, second ed. ISBN 0-19-512999-7.

Gao, K., Wu, J., Zhang, P., Lemmon, E. W., 2016. A Helmholtz energy equation of state for sulfur dioxide. *J. Chem. Eng. Data* 61 (8), 2859–2872. doi:10.1021/acs.jced.6b00195.

Gernert, J., Span, R., 2016. EOS-CG: A Helmholtz energy mixture model for humid gases and CCS mixtures. *J. Chem. Thermodyn.* 93, 274–293. doi:10.1016/j.jct.2015.05.015.

Hammer, M., Aasen, A., Øivind Wilhelmsen, 2024. Extrapolating into no man's land enables accurate estimation of surface properties with multiparameter equations of state. *Fluid Phase Equilib.* 586, 114196. doi:10.1016/j.fluid.2024.114196.

Hammer, M., Deng, H., Austegard, A., Log, A. M., Munkejord, S. T., Nov. 2022. Experiments and modelling of choked flow of CO_2 in orifices and nozzles. *Int. J. Multiphase Flow* 156, 104201. doi:10.1016/j.ijmultiphaseflow.2022.104201.

Hammer, M., Log, A. M., Deng, H., Austegard, A., Munkejord, S. T., 2025. Decompression-induced condensation of carbon dioxide: Experiments, and prediction of supercooling limit using classical nucleation theory – dataset. Zenodo. doi:10.5281/zenodo.14392001.

Herrig, S., Nov. 2018. *New Helmholtz-Energy Equations of State for Pure Fluids and CCS-Relevant Mixtures*. Phd thesis, Ruhr-Universität Bochum. doi:10.13154/294-6284.

Hugill, J., Van Welsenes, A., Oct. 1986. Surface tension: A simple correlation for natural gas + conensate systems. *Fluid Phase Equilib.* 29, 383–390. ISSN 03783812. doi:10.1016/0378-3812(86)85038-5.

IEA, 2022. *World Energy Outlook 2022*. IEA, Paris. URL `https://www.iea.org/reports/net-zero-by-2050`.

Kashchiev, D., 2000. *Nucleation: Basic Theory with Applications*. Butterworth Heinemann, Oxford ; Boston. ISBN 978-0-7506-4682-6.

Kulmala, M., Viisanen, Y., 1991. Homogeneous nucleation: Reduction of binary nucleation to homomolecular nucleation. *J. Aerosol Sci.* 22, S97–S100. ISSN 00218502. doi:10.1016/S0021-8502(05)80043-6.

Kunz, O., Wagner, W., October 2012. The GERG-2008 wide-range equation of state for natural gases and other mixtures: An expansion of GERG-2004. *J. Chem. Eng. Data* 57 (11), 3032–3091. doi:10.1021/je300655b.

Log, A. M., Diky, V., Huber, M. L., 2023. Assessment of a Parachor Model for the Surface Tension of Binary Mixtures. *Int. J. Thermophys.* 44. doi:https://doi.org/10.1007/s10765-023-03216-z.

Log, A. M., Hammer, M., Deng, H., Austegard, A., Hafner, A., Munkejord, S. T., Jan. 2024a. Depressurization of CO_2 in pipes: Effect of initial state on non-equilibrium two-phase flow. *Int. J. Multiphase Flow* 170, 104624. doi:10.1016/j.ijmultiphaseflow.2023.104624.

Log, A. M., Hammer, M., Munkejord, S. T., 2024b. A flashing flow model for the rapid depressurization of CO_2 in a pipe accounting for bubble nucleation and growth. *Int. J. Multiphase Flow* 171. doi:10.1016/j.ijmultiphaseflow.2023.104666.

Mahgerefteh, H., Brown, S., Martynov, S., Oct. 2012. A study of the effects of friction, heat transfer, and stream impurities on the decompression behavior in CO_2 pipelines. *Greenh. Gas. Sci. Tech.* 2 (5), 369–379. doi:10.1002/ghg.1302.

Maxey, W. A., 1983. *Final report on gas expansion studies to American Gas Association*. NG-18 113, BATTELLE Columbus Laboratories, 505 King Avenue Columbus, Ohio 43201.

Michal, G., Davis, B., Østby, E., Lu, C., Røneid, S., Sep. 2018. CO2SAFE-ARREST: A full-scale burst test research program for carbon dioxide pipelines – Part 2: Is the BTCM out of touch with dense-phase CO_2? In: *12th International Pipeline Conference, IPC 2018*. ASME. doi:10.1115/IPC2018-78525.

Michal, G., Østby, E., Davis, B. J., Røneid, S., Lu, C., Sep. 2020. An empirical fracture control model for dense-phase CO_2 carrying pipelines. In: *13th International Pipeline Conference, IPC 2020*. ASME. doi:10.1115/IPC2020-9421.

Mulero, A., Cachadiña, I., Parra, M. I., 2012. Recommended Correlations for the Surface Tension of Common Fluids. *J. Phys. Chem. Ref. Data* 41 (4), 14. doi:10.1063/1.4768782.

Munkejord, S. T., Austegard, A., Deng, H., Hammer, M., Stang, H. G. J., Løvseth, S. W., Nov. 2020. Depressurization of CO_2 in a pipe: High-resolution pressure and temperature data and comparison with model predictions. *Energy* 211, 118560. doi:10.1016/j.energy.2020.118560.

Munkejord, S. T., Deng, H., Austegard, A., Hammer, M., Skarsvåg, H. L., Aasen, A., Jul. 2021. Depressurization of CO_2-N_2 and CO_2-He in a pipe: Experiments and modelling of pressure and temperature dynamics. *Int. J. Greenh. Gas Con.* 109, 103361. doi:10.1016/j.ijggc.2021.103361.

Munkejord, S. T., Hammer, M., Løvseth, S. W., May 2016. CO_2 transport: Data and models – A review. *Appl. Energ.* 169, 499–523. doi:10.1016/j.apenergy.2016.01.100.

Neumann, T., Herrig, S., Bell, I. H., Beckmüller, R., Lemmon, E. W., Thol, M., Span, R., Aug. 2023. EOS-CG-2021: A mixture model for the calculation of thermodynamic properties of CCS mixtures. *Int. J. Thermophys.* 44 (178). doi:10.1007/s10765-023-03263-6.

Ohta, S., Jan. 1982. On the rate of homogeneous nucleation in ternary systems. *J. Aerosol Sci.* 13 (2), 139–145. ISSN 00218502. doi:10.1016/0021-8502(82)90059-3.

Porthos, 2023. Project. https://www.porthosco2.nl/en/project/. Accessed 2024-11-04.
Roussanaly, S., Bureau-Cauchois, G., Husebye, J., Jan. 2013. Costs benchmark of CO_2 transport technologies for a group of various size industries. *Int. J. Greenh. Gas Con.* 12, 341–350. doi:10.1016/j.ijggc.2012.05.008.
Schmelzer, J. W. P., Schmelzer, J., Jürn, Gutzow, I. S., 02 2000. Reconciling gibbs and van der waals: A new approach to nucleation theory. *The Journal of Chemical Physics* 112 (8), 3820–3831.
Shukla, P. R., Skea, J., Slade, R., Fradera, R., Pathak, M., Al Khourdajie, A., Belkacemi, M., van Diemen, R., Hasija, A., Lisboa, G., Luz, S., Malley, J., McCollum, D., Some, S., Vyas, P. (Eds.), 2022. *Climate Change 2022: Mitigation of Climate Change. Contribution of Working Group III to the Sixth Assessment Report of the Intergovernmental Panel on Climate Change*. Cambridge University Press, Cambridge, UK and New York, NY, USA. doi:10.1017/9781009157926.
Skarsvåg, H. L., Hammer, M., Munkejord, S. T., Log, A. M., Dumoulin, S., Gruben, G., Mar. 2023. Towards an engineering tool for the prediction of running ductile fractures in CO_2 pipelines. *Process Saf. Environ.* 171, 667–679. doi:10.1016/j.psep.2023.01.054.
Smith, E., Morris, J., Kheshgi, H., Teletzke, G., Herzog, H., Paltsev, S., 2021. The cost of CO_2 transport and storage in global integrated assessment modeling. *Int. J. Greenh. Gas Con.* 109, 103367. doi:https://doi.org/10.1016/j.ijggc.2021.103367.
Stauffer, D., Jul. 1976. Kinetic theory of two-component ("hetero-molecular") nucleation and condensation. *J. Aerosol Sci.* 7 (4), 319–333. doi:10.1016/0021-8502(76)90086-0.
Sugden, S., 1924. A relation between surface tension, density, and chemical composition. *J. Chem. Soc., Trans.* 125, 32–41. doi:10.1039/CT9242501177.
Trinkaus, H., Jun. 1983. Theory of the nucleation of multicomponent precipitates. *Phys. Rev. B* 27 (12), 7372–7378. ISSN 0163-1829. doi:10.1103/PhysRevB.27.7372.
Vehkamäki, H., 2006. *Classical Nucleation Theory in Multicomponent Systems*. Springer, Berlin ; New York. ISBN 978-3-540-29213-5 978-3-540-31218-5.
Vehkamäki, H., Ford, I. J., Aug. 2000. Analysis of water–ethanol nucleation rate data with two component nucleation theorems. *J. Comput. Phys.* 113 (8), 3261–3269. ISSN 0021-9606, 1089-7690. doi:10.1063/1.1286965.
Wedekind, J., Wölk, J., Reguera, D., Strey, R., 10 2007. Nucleation rate isotherms of argon from molecular dynamics simulations. *J. Comput. Phys.* 127 (15), 154515. doi:10.1063/1.2784122.
Weinaug, C. F., Katz, D. L., Feb. 1943. Surface Tensions of Methane-Propane Mixtures. *Ind. Eng. Chem.* 35 (2), 239–246. ISSN 0019-7866, 1541-5724. doi:10.1021/ie50398a028.
Wilemski, G., Wyslouzil, B. E., Jul. 1995. Binary nucleation kinetics. I. Self-consistent size distribution. *J. Comput. Phys.* 103 (3), 1127–1136. doi:10.1063/1.469823.
Wilhelmsen, Ø., Aasen, A., 2022. Choked liquid flow in nozzles: Crossover from heterogeneous to homogeneous cavitation and insensitivity to depressurization rate. *Chem. Eng. Sci.* 248, 117176. doi:10.1016/j.ces.2021.117176.
Wilhelmsen, Ø., Aasen, A., Skaugen, G., Aursand, P., Austegard, A., Aursand, E., Gjennestad, M. A., Lund, H., Linga, G., Hammer, M., 2017. Thermodynamic modeling with equations of state: Present challenges with established methods. *Ind. Eng. Chem. Res.* 56 (13), 3503–3515. doi:10.1021/acs.iecr.7b00317.

Appendix A. Decompression-speed plots of previously published experimental data

In this section, decompression plots are presented for all experiments available in the literature. Except for the experiments of Munkejord *et al.* (2020) and Botros *et al.* (2017a), where experimental data were directly available, the decompression speed versus pressure curves were digitally extracted from the source articles. The pure CO_2 experiments are shown first in Figures A.1 and A.2, while the CO_2-rich mixture experiments are presented in Figures A.3 to A.5.

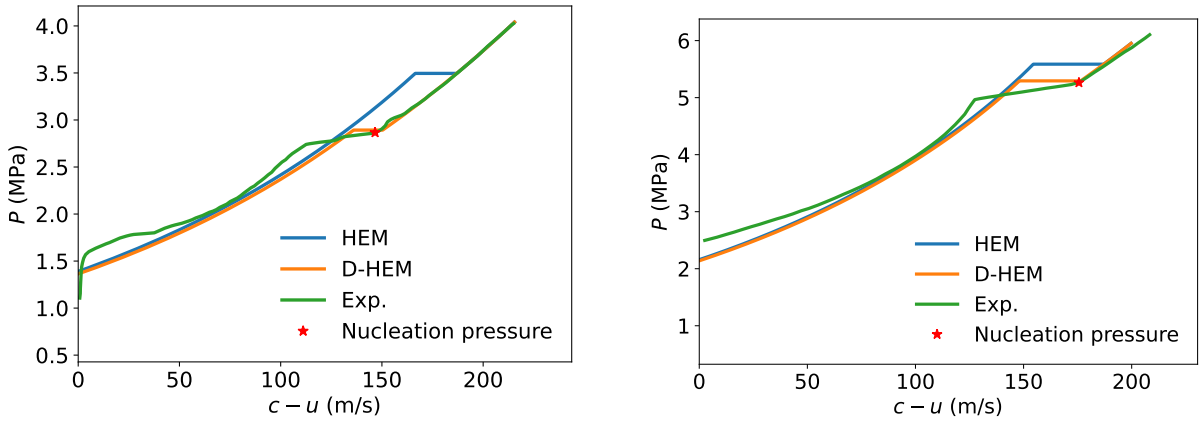

(a) Experiment of Munkejord *et al.* (2020).

(b) Experiment of Maxey (1983).

Figure A.1: Pure CO_2 decompression speeds (green), compared to HEM (blue) and D-HEM (orange) results. The experimentally derived nucleation pressure is indicated as a red star.

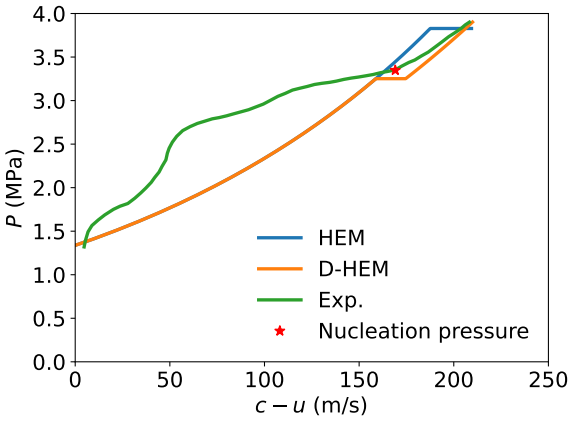

(a) Test 02.

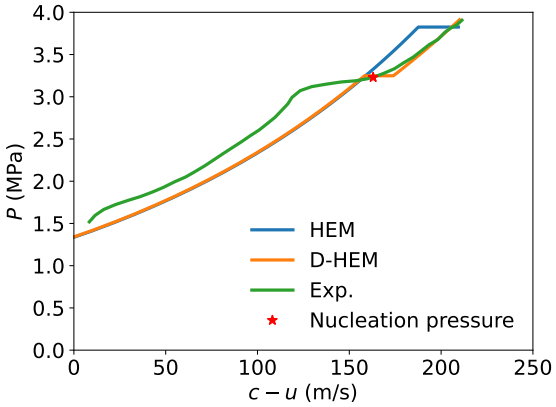

(b) Test 03.

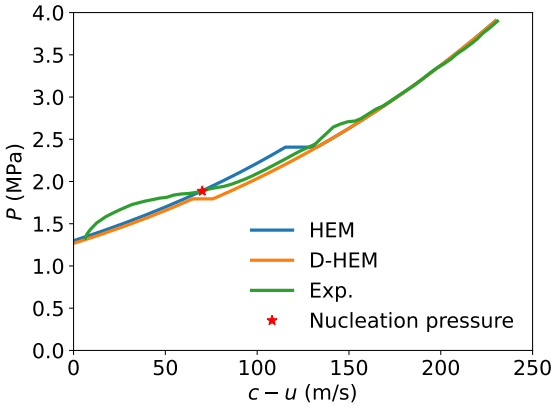

(c) Test 04.

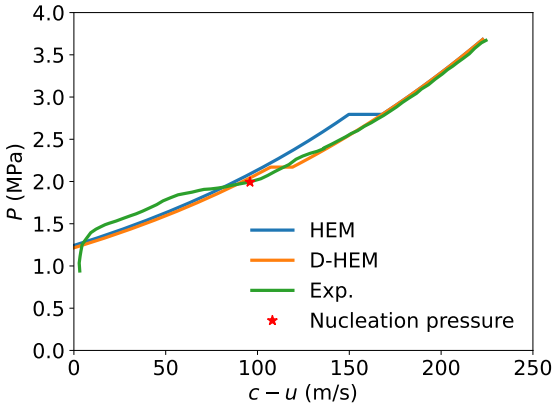

(d) Test 13.

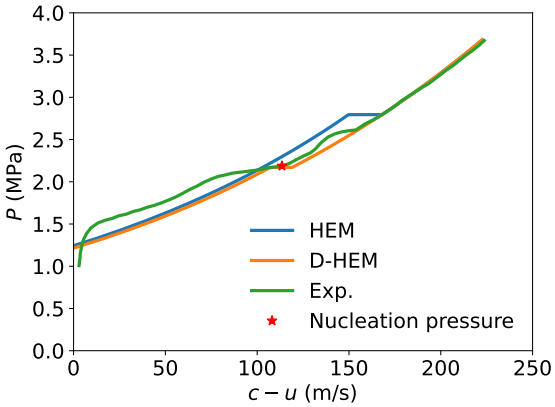

(e) Test 14.

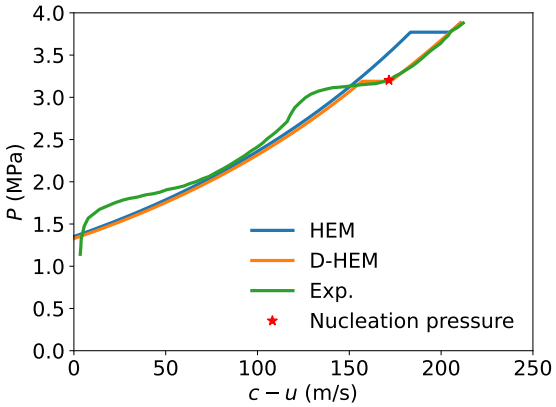

(f) Test 16.

Figure A.2: Pure CO_2 decompression speeds from Cosham *et al.* (2011) (green), compared to HEM (blue) and D-HEM (orange) results. The experimentally derived nucleation pressure is indicated as a red star.

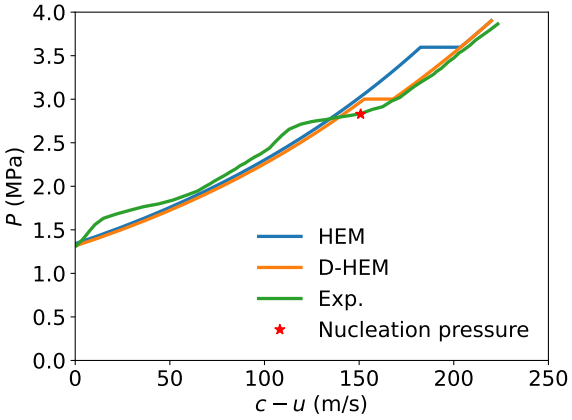

(a) Test 05 (97.0% CO_2, 3.0% H_2).

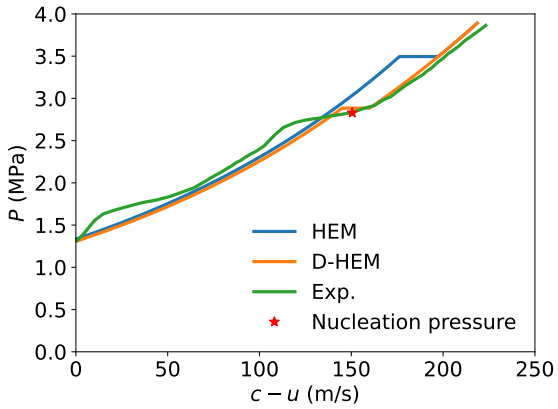

(b) Test 06 (96.0% CO_2, 4.0% N_2).

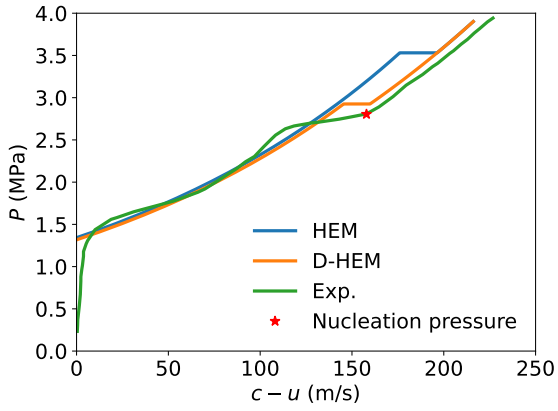

(c) Test 07 (99.1% CO_2, 0.9% SO_2).

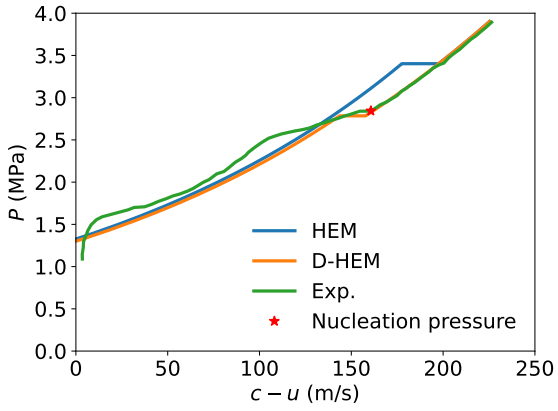

(d) Test 08 (95.7% CO_2, 3.3% H_2, 1.0% SO_2).

Figure A.3: CO_2-mixture decompression speeds from Cosham *et al.* (2011) (green), compared to HEM (blue) and D-HEM (orange) results. The experimentally derived nucleation pressure is indicated as a red star.

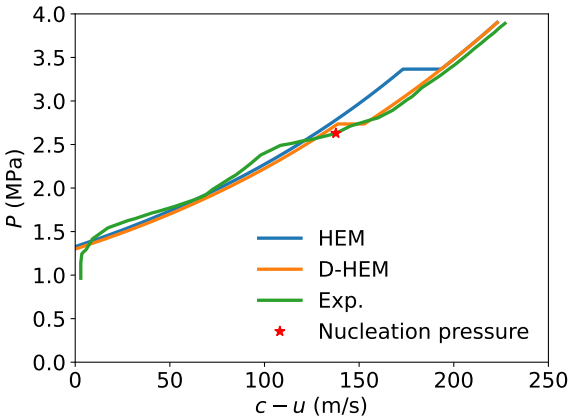

(a) Test 09 (94.8% CO_2, 4.2% N_2, 1.0% SO_2).

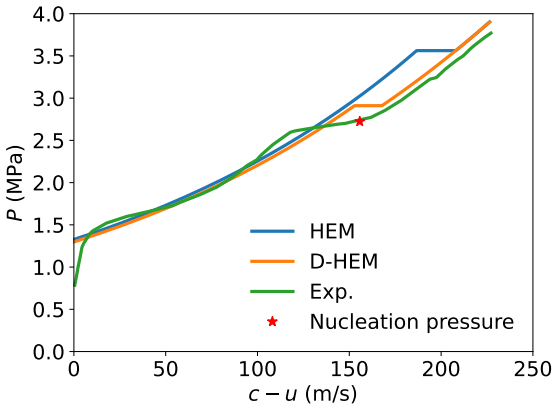

(b) Test 10 (88.9% CO_2, 7.9% N_2, 1.1% O_2, 1.1% CH_4, 1.0% SO_2).

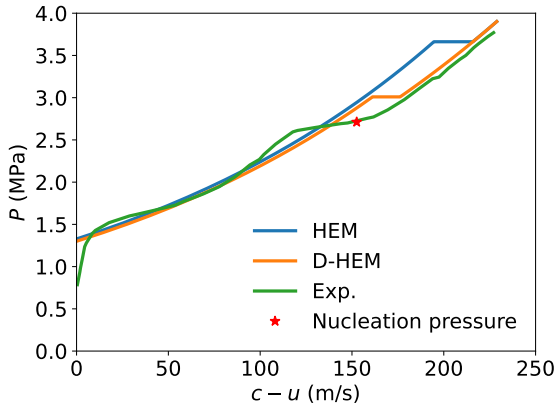

(c) Test 11 (89.4% CO_2, 3.2% H_2, 3.8% N_2, 1.3% O_2, 1.1% CH_4, 1.2% SO_2).

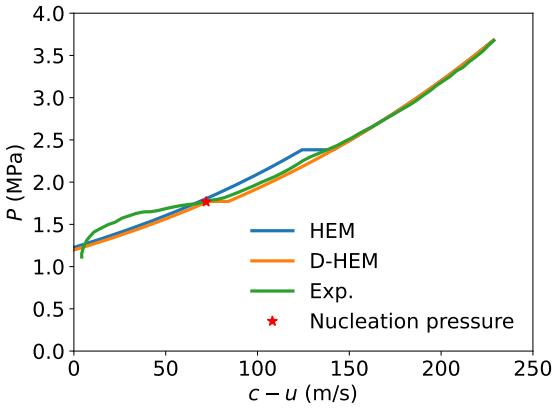

(d) Test 12 (95.7% CO_2, 3.3% H_2, 1.0% SO_2).

Figure A.4: CO_2-mixture decompression speeds from Cosham *et al.* (2011) (green), compared to HEM (blue) and D-HEM (orange) results. The experimentally derived nucleation pressure is indicated as a red star.

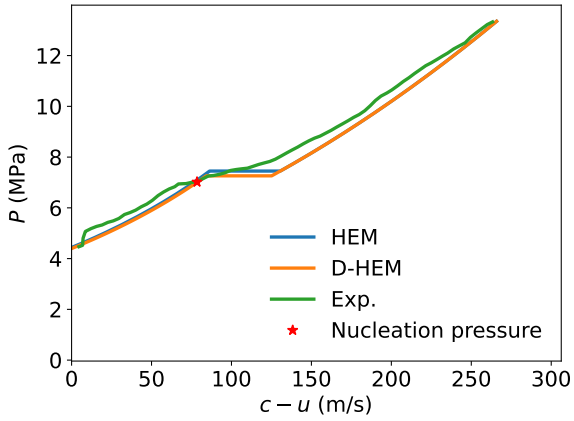

Figure A.5: Decompression speed of a 83.3% CO_2, 3.5% N_2, 5.8% O_2, 7.4 % Ar mixture by Botros *et al.* (2017a) (green), compared to HEM (blue) and D-HEM (orange) results. The experimentally derived nucleation pressure indicated as a red star.